Nature of radio echo layering in the Antarctic ice sheet detected by a two-frequency experiment

Shuji Fujita,[1] Hideo Maeno,[2] Seiho Uratsuka,[2] Teruo Furukawa,[3] Shinji Mae,[1] Yoshiyuki Fujii,[3] and Okitsugu Watanabe[3]

Abstract. A two-frequency radio echo sounding experiment was carried out at Dome Fuji, the second highest dome in East Antarctica, and along a 1150-km-long traverse line from the dome to the coast. The goal was to determine the dominant causes of the radio echo internal reflections and to investigate their possible changes with depth ranges and regions. From the two-frequency (60 MHz and 179 MHz) radio echo responses at various sites, we distinguished four zones. Each of the zones is characterized by a dominant cause of radio echo internal reflection as follows. In the "P_D" zone, changes in dielectric permittivity are mainly due to density fluctuations; in the "P_{COF}" zone, changes in dielectric permittivity are mainly due to changes in crystal-orientation fabrics; and in the "C_A" zone, changes in electrical conductivity are mainly due to changes in acidity induced by past volcanic eruptions. In each of these three zones, the changes occur commonly along isochrones. In addition, a basal echo-free zone, the fourth zone, was found to appear always below the P_{COF} zone. These four zones and their distribution suggested variations of the physical conditions within the ice sheet.

1. Introduction

In the Antarctic ice sheet, mass inputs (snow accumulation) are transported by ice flow to outlet ice streams and glaciers and/or to ice shelves. Timescales for this transport can vary from the order of 10^2 to 10^5 years depending on the physical processes operating within the ice sheet. Therefore understanding of the physical processes and flow regime is of great importance for interpreting past, present, and future changes of the ice sheet.

To investigate subsurface properties of the large ice masses, radar sounding techniques have been used for several decades at frequencies between a few and several hundred megahertz as a powerful tool [Bogorodskiy et al., 1985; Robin et al., 1969]. Reflections of radio waves from within the ice are caused by sudden changes in complex dielectric permittivity of layers in the ice sheets. Since the first report of internal layers [Bailey et al., 1964], various mechanisms have been suggested and investigated [Ackley and Keliher, 1979; Clough, 1977; Fujita and Mae, 1994; Gudmandsen, 1975; Harrison, 1973; Jacobel and Hodge, 1995; Millar, 1981; Miners et al., 1997; Moore, 1988; Paren and Robin, 1975; Robin, 1975; Robin et al., 1969; Robin and Millar, 1982]. From all these papers, three mechanisms have emerged as possible causes of the sudden changes: changes in (1) density, (2) acidity, and (3) crystal-orientation fabrics. However, the mechanisms have often been interpreted differently from one paper to another. The common understanding at present is that in the top several hundred meters of the ice sheet the permittivity variations are

dominated by changing density (hereafter we describe this mechanism as P_D("P" for permittivity and "D" for density)). Near the surfaces of the ice sheets, extensive melting, depth hoar, or precipitation hiatuses can cause changes in density large enough to create strong reflections. However, in deeper layers, the reflections cannot be explained by the P_D mechanism because of the densification of ice and phase transition of air bubbles into clathrate hydrate crystals.

In some studies, several of the internal reflection layers are correlated to depths corresponding to the dates of large volcanic eruptions [Millar, 1981]. Hammer [1980] has shown that a volcanic eruption can increase the level of acidity in precipitation in polar regions for one or more years after the eruption. Therefore, until recently, in many papers the cause of internal reflections from deeper layers has been assigned simply to changes in electrical conductivity due to changes in acidity (hereafter we describe this mechanism as C_A("C" for conductivity and "A" for acidity)). Laboratory measurements of the electrical conductivity of ice containing strong acids at microwave frequencies and low frequencies [Fujita et al., 1992a; K. Matsuoka et al., 1996; Matsuoka et al., 1997a; Moore and Fujita, 1993] have also demonstrated that the C_A mechanism can cause detectable reflections.

Recently, a series of dielectric measurements [Fujita et al., 1993; Fujita et al., 1992b; Matsuoka et al., 1997b] gave the magnitude of dielectric anisotropy in ice Ih (hexagonal) crystals. The magnitude is great enough to suggest that changes in permittivity due to changes in crystal orientation fabrics (hereafter we describe this mechanism as P_{COF}("P" for permittivity and "COF" for crystal-orientation fabrics)) can also produce detectable reflections [Fujita and Mae, 1994].

Since radio echo reflections due to the two factors, dielectric permittivity (P_D and P_{COF}) and electrical conductivity (C_A), have different responses with frequency change, we proposed that multifrequency radar sounding would be a viable experimental method to clarify the dominant causes of internal reflections [Fujita and Mae, 1994]. In 1990-1998, the Japanese Antarctic Research Expedition conducted a deep ice

---

[1] Department of Applied Physics, Faculty of Engineering, Hokkaido University, Sapporo, Japan
[2] Communications Research Laboratory , Ministry of Post, Tokyo.
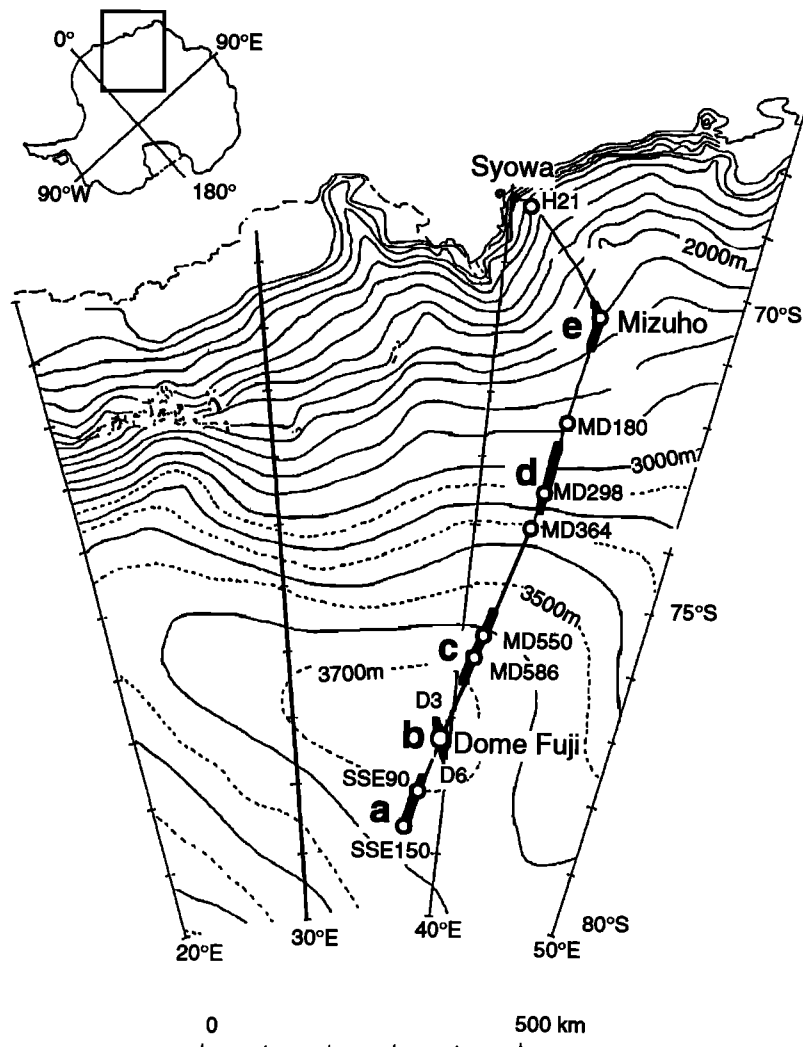[3] National Institute of Polar Research, Tokyo.

Figure 1. Elevation map of East Antarctica, showing the location of the 1150-km-long traverse route from the site "SSE150" through Dome Fuji to the coast. Circles indicate sites of detailed local measurements. The five bold lines (indicated by a-e) are sections of the traverse line used in cross-section analyses in Figures 2 and 3, and Plate 2. Note that line b is at an angle to the profile line of Figure 2.

coring project at Dome Fuji, the second highest dome in East Antarctica (77°19'S; 39°40'E; 3810 meters above sea level, and ice thickness 3028 (±15) m). A 2504-m-long core containing about 350,000 annual precipitation layers was recovered (Dome F Ice Core Research Group, personal communication, 1998). During the long-term coring effort, radar sounding operations were carried out twice. The first time, in 1991-1993, was to make a subglacial bed-map in the search for the best site for the deep coring [*Maeno et al.*, 1994, 1996]. The second (present study) was performed in 1995-1997 to investigate the internal structure of the ice sheet at the two frequencies, 60 MHz and 179 MHz. In order to clarify the causes of internal reflections and their possible variations in ice, the ice sheet internal reflections were investigated along a 1150-km-long traverse line from a site 150 km SSE of Dome Fuji to the coast near Syowa station (Figures 1 and 2).

This paper reports the major results to date and will show that by radar sounding we can assess and interpret the internal physical processes and their changes, one of the most important keys to interpreting mass balance. Details, such as relation between internal reflection layers and ice core signals, detailed regional features, and polarization effects, will be reported elsewhere.

2. Experiment

2.1. Basic principle

2.1.1. Basic equations. The method to discriminate dominant reflections due to dielectric permittivity (P_D and P_{COP}) and electrical conductivity (C_A) is based on the complex dielectric properties of ice Ih crystals. Depending on the dominant cause of reflections (permittivity or conductivity), the resulting power reflection coefficients follow different equations. For convenience, we express the power reflection coefficients due to permittivity and due to conductivity as R_p and R_c, respectively. The subscripts denote the reflection mechanisms. At a flat boundary, R_p and R_c are proportional to the square of the changes in permittivity ($\Delta\varepsilon$) or conductivity ($\Delta\sigma$), respectively, as follows [*Fujita and Mae*, 1994; *Paren*,
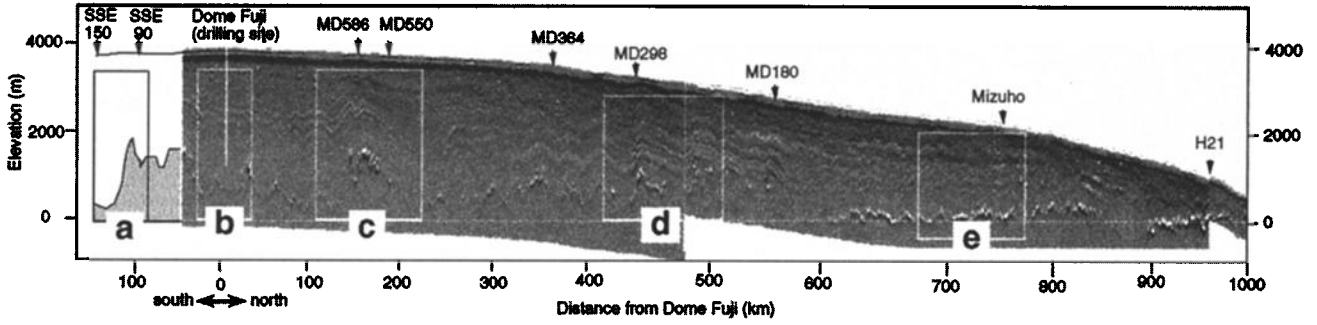
Figure 2. Cross section map of the ice sheet along the 1150 km traverse line. Z-scope images (radar returns versus both depth and distance along the traverse) are from *Maeno et al.* [1994, 1996]. The 10 sites of detailed local measurements and the five areas (a-e) of cross section analyses are indicated. Note that the image is the first derivative of the received power along depth based on the 179-MHz measurement using a 1000-ns pulse. The section southeast of SSE40 was not measured.

1981; *Paren and Robin,* 1975]:

$$R_p \propto \Delta\varepsilon^2 \tag{1a}$$

$$R_c \propto \left(\frac{\Delta\sigma}{f}\right)^2. \tag{1b}$$

Here f is the frequency of electromagnetic waves. Equation (1a), which expresses the effect of permittivity, holds in the cases of P_D and P_{COF}. The discrimination between P_D and P_{COF} arises later in the analysis (see section 4). Equation (1b), which expresses the effect of conductivity, holds in the case of C_A. For all three mechanisms, $\Delta\varepsilon$ and $\Delta\sigma$ are independent of f in the frequency range used for radar sounding (from 1 MHz to several hundred megahertz) and in the temperature range of polar ice sheets [see *Evans,* 1965; *Matsuoka et al.,* 1997b; *Moore and Fujita,* 1993; *Warren,* 1984]. The important difference between R_p in (1a) and R_c in (1b) is that only R_c is inversely proportional to the square of f. Therefore, if two frequencies (hereafter f_1 and f_2) are used for radar sounding, the reflections due to C_A can be distinguished from the reflections due to P_D or P_{COF} by observing whether the power reflection coefficients follow (1a) or (1b) [*Fujita and Mae,* 1994].

The quantity usually observed in radar is a time series of received power and not the power reflection coefficients. Therefore we consider the relation between the received power and the power reflection coefficients as follows. In the actual radar measurement, the relation between the power (P_R) received from the receiver antenna and the reflection from targets is described by a radar equation. If the reflection from the surface is calculated using Fresnel reflection, the radar equation is [e.g. *Bogorodskiy et al.,* 1985],

$$P_R = \frac{P_T G^2 \lambda^2 q R}{64 \pi^2 z^2 L}, \tag{2}$$

where P_T is the transmitted power; R is the power reflection coefficient, that is, R_p or R_c; G, λ, and q are antenna gain, wave length in vacuum, and "refraction gain", respectively, which express an effect of modification of beam width by refraction at the air/ice interface; L is the loss factor due to energy absorption (note that transmission loss which occurs at each internal layer interface due to reflections is negligibly small); and z is the depth to the reflector retrieved from travel time of electromagnetic waves in ice. L is a function of z and is dependent on temperature.

Equation (2) assumes an idealized situation in which the interfaces are smooth planes, so no scattering takes place. This assumption has been widely used in most of the previous studies on ice sheet internal reflections. In the nonidealized case, that is, when the scattering component from an undulating surface or slightly rough surface cannot be ignored, we should use a different form of the radar equation. In this case, a scattering cross-section factor appears in the equation and requires the use of one of the two widely known theories, the surface scattering theory of Kirchhoff or the small-perturbation method [*Ulaby et al.,* 1982]. Nevertheless, in each scattering model, the scattering cross section is commonly proportional to the power reflection coefficient; hence P_R is still proportional to the power reflection coefficient, as in (2). This point is the basis of the following analysis.

Using (2), we define the relative magnitude of P_R detected by the two-frequency radar systems at common depths on a decibel scale as follows:

$$\Delta P_R = 10 \log_{10}\left(\frac{P_R(f_1)}{P_R(f_2)}\right)$$

$$= 10 \log_{10}\left(\frac{R(f_1)}{R(f_2)}\right) + C. \tag{3}$$

Here C is a number determined by the parameters λ, P_T, and G. Note that both q and L are independent of frequency in the frequency range up to several hundred megahertz, according to a recent update of complex permittivity data for ice [*T. Matsuoka et al.,* 1996]. The motivation for factoring out this frequency dependence into a separate term C is that it is independent of the physical process giving rise to the echoes. If we can ignore the value of C in (3), we can obtain values of ΔP_R that are a function of only the echo-producing processes. If the dominant cause of reflection is P_D or P_{COF}, the first term of ΔP_R becomes 0 (decibels) according to (1a), and if the dominant cause of reflection is C_A, the first term of ΔP_R becomes $10 \log_{10}(f_2/f_1)^2$ (decibels) according to (1b). Therefore we can distinguish the P_D/P_{COF} reflections from the C_A reflections in the ice column by observing changes with depth of ΔP_R by a magnitude of $10 \log_{10}(f_2/f_1)^2$ (decibels) since the second term will be a constant difference assuming that we fix the parameters λ, P_T, and G for each radar. In the

Table 1. Specifications of the Two Radar Systems Used in This Experiment.

		Frequency	
	Parameter	60 MHz	179 MHz
Transmitter	peak power	1 kW	1 kW
	pulse width	250 ns	350 ns / 150 ns
	resolution in ice	21 m	30 m / 13 m
	wavelength in ice	2.8 m	0.94 m
	repetition period	1 ms	1 ms
Receiver	sensitivity	-110 dBm *	-110 dBm
	bandwidth	4 MHz	4 MHz / 14 MHz
	noise figure	< 1 dB	< 1 dB
Antenna	type	three element Yagi (x 2)	three element Yagi (x 2)
	gain	7.2 dBi †	8.15 dBi

* Here dBm is a unit for expression of power level in decibels with reference to a power of 1 mW.

† Here dBi is a unit for expression of antenna gain in decibels with reference to a power of an ideal isotropic antenna. We need to use this unit and definition in calculations of antenna gain in the radar equations.

present case, f_1 and f_2 are 179 MHz and 60 MHz, respectively, so the magnitude of the change is about 9.5 dB. This value means that permittivity-based reflections cause ΔP_R to be about 10 dB larger than that of conductivity-based reflections.

2.1.2. Possible sources of error. There are two factors of unavoidable error in determining the values in (3). They are (1) the interference effect of two or more reflections in a radar pulse that are several tens of meters long [*Fujita and Mae*, 1994; *Harrison*, 1973] and (2) a coupling effect between the antennae and the ice sheet surface. The former error can happen because each reflection layer has limited thickness. Reflections occur both at the upper and lower boundaries of a layer. In addition, if there are two or more layers in a radar pulse, interference of radio waves from four or more reflections occurs. From this point of view, what we are observing by ice radar are interference patterns from many reflections and not simple addition of reflections [*Jacobel and Hodge*, 1995; *Moore*, 1988]. This interference effect is a complex function of both frequency and distances between reflectors. However, if the distances between reflectors are randomly distributed, this will appear only like a random error. This error can cause some fluctuations in the time series of the received power, but it does not affect the mean tendency of the signal level. According to the simulations that we carried out (creating radargrams by calculation based on ice core data), the magnitude of the fluctuations is of the order of several decibels.

The coupling-effect error can happen because the return signal from shallow depths (in particular from the air/ice boundary) to the antennae interferes with the antennae. Consequently, both radiation pattern and antenna gain G are affected. Gain in Table 1 assumes that there is no such interference. This assumption is not correct in the case of ground-based measurements because the first major reflector (the air/ice boundary) is too close to be ignored. However, since this effect is a function primarily of both frequency and antennae height and both are almost constant throughout our measurements, it appears as a constant value and does not affect our discrimination procedure between permittivity- and conductivity-based reflections.

In summary, (3) holds for reflections from smooth and slightly rough surfaces. What we are examining is the relative variation of ΔP_R with depth, and in particular, we are interested in regions where it changes by about 10 dB.

2.2. Radar Systems

The radar systems at 179 MHz and 60 MHz have been developed by the National Institute of Polar Research and the Communications Research Laboratory. The specifications are listed in Table 1. Both systems have the same transmission power (1 kW) and similar antenna patterns with three-element Yagi antennae. The small difference in pulse width, 350 or 150 ns for the 179-MHz system and 250 ns for the 60-MHz system, will influence the ΔP_R by no more than a few decibels,

Table 2. Sites for Point Measurement.

| Site	Position Latitude (South)	Longitude (East)	Altitude*	Note
(a) SSE150	78°41'	37°47'	3722	inland of Dome Fuji, above the subglacial basin
(b) SSE90	78°10'	38°31'	3765	inland of Dome Fuji, above the subglacial mountains
(c) Dome Fuji	77°19'	39°42'	3810	Dome Fuji summit, deep coring site
(d) MD586	76°00'	41°11'	3693	in front of a subglacial mountain
(e) MD550	75°41'	41°32'	3623	behind the subglacial mountain
(f) MD364	74°01'	43°00'	3353	
(g) MD298	73°25'	43°15'	3202	above the subglacial mountains
(h) MD180	72°22'	43°42'	2833	above the subglacial mountains
(i) Mizuho	70°42'	44°17'	2250	
(j) H21	69°06'	40°48'	1076	close to the coast

* Altitude is meters above sea level.
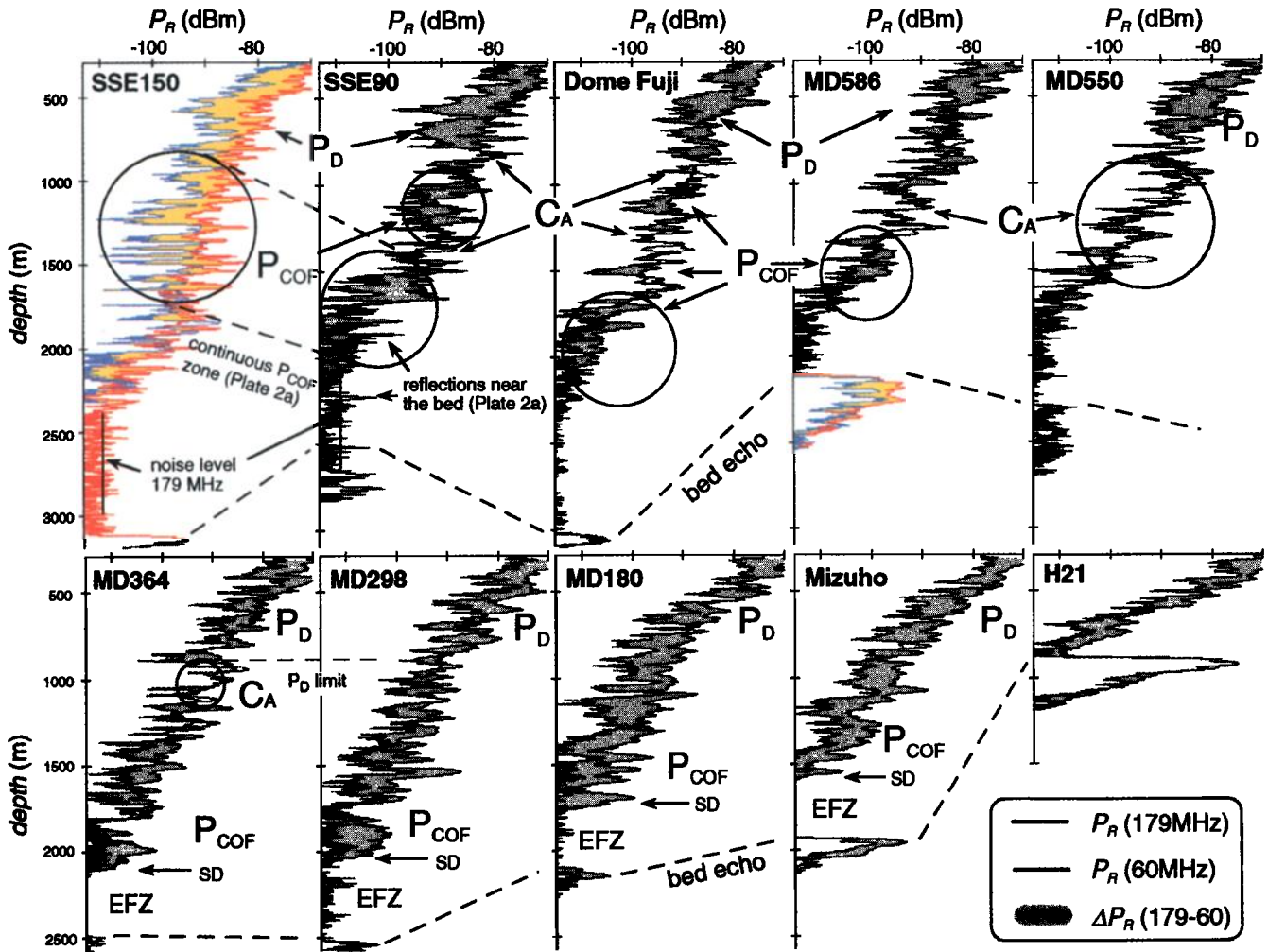
Plate 1. A-scope profiles at the 10 sites of detailed local measurements. Red and blue lines are $P_R(179)$ and $P_R(60)$, respectively. The variation of ΔP_R (equal to $P_R(179)$ - $P_R(60)$) with depth is shown in yellow. The dominant reflection mechanisms at various depth ranges are shown as P_D, P_{COF}, and C_A (see section 4). Detection limit (noise level) is at about -110 dBm. The profiles below this level are noise. Only when sudden drop of the signal is observed at transitions between significant signal and noise (indicated by "SD"), the depth range of the noise level is defined as the basal echo-free zone. It is indicated as EFZ.

which does not seriously affect the discrimination between the two mechanisms P_{COF} /P_D and C_A. The radar systems were regularly and precisely calibrated during the experiment to ensure long-term stability of system performance. The radar systems were mounted on two snow vehicles [*Maeno et al.*, 1994, 1996]. The transmitting and receiving antennae were set on opposite sides of each vehicle. They were kept parallel to the vehicle axis and separated by a distance of 6.4 m from one another. The centers of the antennae were 3.2 m above the ice sheet surface. All the data were digitally recorded with a digital oscilloscope and a portable computer linked through GPIB (General Purpose Interface Bus).

2.3. Observation Sites and Data Sampling

The observational sites are indicated on the map in Figure 1, and the cross section is shown in Figure 2. The 1150-km traverse route started from a site located 150 km SSE from the Dome Fuji, going through both Dome Fuji and Mizuho station, to reach the coast. This route does not exactly follow the flow line because it was prepared as a logistic route (for

transportation between stations). During the traverse, the radio echo data were continuously recorded, and the antennae were always oriented along the traverse line. On the traverse route, 10 sites (Table 2) were selected for point measurements in order to obtain a better signal/noise ratio for signals in deeper layers by averaging data over a longer time period. These sites are characterized by a variety of subglacial bedrock conditions and ice sheet flow conditions (see Figure 2 and Table 2). Anticipating future studies on the effect of polarization, the antennae were also rotated stepwise by 22.5° for 8 orientations or 11.25° for 16 orientations, but the results of this investigation are not developed here.

3. Results

A value of -7.6 dB was added systematically to all values of P_R at 60 MHz (henceforth called $P_R(60)$) to compensate for the difference in antenna parameters G and λ in (2). P_R at 179 MHz (henceforth called $P_R(179)$) as slightly corrected (by less than 2.2 dB) to account for the difference in pulse length in the radar systems. The accidental (statistical) errors both in
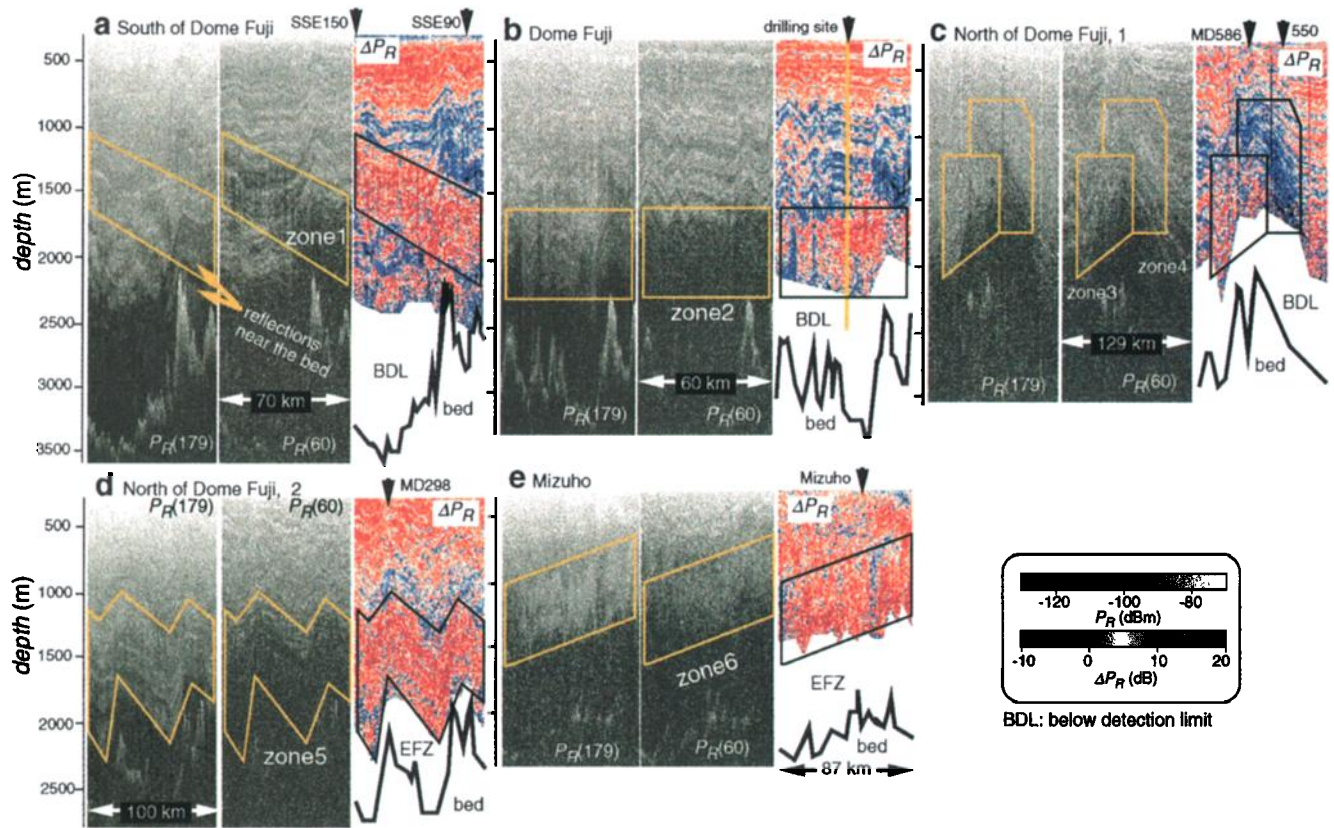
Plate 2. Z-scope profiles at sites a-e (Figures 1 and 2): (a) south of Dome Fuji, (b) Dome Fuji, (c) North of Dome Fuji 1, (d) north of Dome Fuji 2, and (e) Mizuho. Note that profile of Plate 2b, at Dome Fuji is at an angle to the profile line of Figure 2 (see Figure 1). For each site, there are cross sections of $P_R(179)$ and $P_R(60)$ in black and white and ΔP_R in color. ΔP_R changes between about 10 dB (red) and about 0 dB (blue) depending on the dominant reflection mechanisms: permittivity (P_D and P_{COF}) or conductivity (C_A), respectively. The zones 1~6 on Plate 2 are discussed in the text. At white zones indicated by "BDL", signals were below the detection limit. ΔP_R is not significant there. In Plates 2d and 2e, BDL is the same as the basal echofree zone (EFZ).

$P_R(179)$ and $P_R(60)$ are less than 1 dB. Therefore the errors in the relative variation of ΔP_R (equal to $P_R(179) - P_R(60)$) with depth are less than 1.4 dB.

The data are presented in two kinds of plates. First, 10 A-scope traces (a display format for showing profiles of radar intensity versus depth) recorded at the 10 point-measurement sites are presented to give a large-scale overview of the ice sheet structure. Second, Z-scope profiles (a display format for showing radar intensity versus both depth and position) of five selected areas of (a-e in Figure 2) about 60-130 km wide are shown to depict local features of the ice sheet structure.

3.1.   Large-Scale Features

Plate 1 shows the variation of P_R at the two frequencies, $P_R(179)$ and $P_R(60)$ (dBm), and the difference between them, ΔP_R (in decibels). Note that the unit of received power, P_R is dBm, the unit for the expression of power levels in decibels with reference to a power of one mW. In contrast, the unit of ΔP_R is in decibels, which simply expresses the relative ratio of magnitude between two P_R values in decibel scale. Note that detection limit (noise level) is at about -110 dBm. Profiles below this level are basically noise and are not significant.

3.1.1.   Changes in $P_R(179)$ and $P_R(60)$. As a general tendency, both $P_R(179)$ and $P_R(60)$ decrease with depth because of increase of both depth z and the loss factor L in the radar equation (2). Generally, $P_R(60)$ shows larger fluctuations

than $P_R(179)$, especially below a depth of about 700 m. $P_R(179)$ is clearly stronger than $P_R(60)$ at depths just above the echo-free zone (EF zone or EFZ) at sites MD364 to Mizuho; it then suddenly drops at a limit indicated by "SD" into the EFZ. At sites SSE150 to MD550, both $P_R(179)$ and $P_R(60)$ reach the noise level of about -110 dBm before showing any EF zone. At site SSE90, a few significant reflections appear from the noise level, indicated as "reflections near the bed" on Plate 1. We particularly mention these reflections because they are internal reflections that occurred exceptionally near the bed (about 2300 m). In addition, these reflections were stronger near the subglacial bed peaks (see location of the site in Figure 2) than away from the peak. This special condition can suggest the cause of these reflections.

3.1.2.   Changes in ΔP_R. In Plate 1, ΔP_R is represented by the area between $P_R(179)$ and $P_R(60)$. When $\Delta P_R > 0$, the area is colored yellow. First, we observe that the magnitude of ΔP_R varies from initial values of about 10 dB to values of about 0 dB. Those absolute values of ΔP_R are larger than the values predicted from (3) (from 0 dB to -10 dB). This means that C in (3) is larger in magnitude by about 10 dB than the -7.6 dB correction applied. Consequently, $\Delta P_R = 10$ dB if the dominant cause of reflection is P_D or P_{COF} (the frequency-independent cases in (1a)), and $\Delta P_R = 0$ dB if the dominant cause of reflection is C_A (the frequency-dependent case in

(1b)). A possible reason for this large value of C could be systematic errors in G due to the coupling effect, as we discussed in section 2.1.2.. Nevertheless, the variation of ΔP_R is generally in good agreement with the theory. Note that ΔP_R is still significant even when $P_R(60)$ is below the detection limit (-110 dBm), as far as $P_R(179)$ is above it. In this case, we can still detect whether ΔP_R is around zero or larger. As a general observation, $\Delta P_R \simeq 10$ dB in the first several hundred meters of the ice sheet on each of the profiles, approximately down to 700-900 m. However, $\Delta P_R \simeq 10$ dB can also be seen at deeper depths. From the coast to inland as far as MD364, ΔP_R is dominantly about 10 dB; the yellow area appears almost continuously above the EF zone. At MD550, the yellow area suddenly disappears below about 700-900 m, showing that ΔP_R has dropped to about 0 dB. From MD586 to SSE90, large zones of $\Delta P_R \simeq 0$ dB and $\Delta P_R \simeq 10$ dB appear alternately.

3.2. Local-Scale Features

Plate 2 is a set of Z-scope images for continuous measurements along segments (a-e in Figures 1 and 2) of the traverse line. The width of the zones varies from about 60 km to 130 km, generally oriented approximately along the ice flow (note that the vertical exaggeration varies between about 60 and 130). Plate 2 gives information on local features that is complementary to that in Plate 1. At each site, there is a two-dimensional representation of $P_R(60)$ and $P_R(179)$ in gray scale and of ΔP_R in color. Note again that ΔP_R is still significant even when $P_R(60)$ is below the detection limit (-110 dBm), as far as $P_R(179)$ is above it. On most of Plate 2, there are clear reflections from the bed. Above that, there is an area (white zone indicated as BDL or EFZ) and then a lighter zone in which we can see the internal reflection features. Note that the basal echo-free zone (EFZ) is a special case of depth range of noise level (below detection level (BDL)) above which a sudden drop of the $P_R(179)$ was observed (see Plate 1). Generally, $P_R(60)$ shows better feature contrast than $P_R(179)$, but $P_R(179)$ illuminates at greater depths. We next describe detailed features of reflections in each segment. Plates 2a-2e show that these features strongly depend on the geographical location of the record (see Figure 2 and Table 2). These results imply that changes in physical processes related to the echo-producing mechanism take place.

In Plate 2a, we see changes in reflection amplitudes in the sections above the subglacial peaks (on the right) and above a subglacial basin (on the left). Ice flows from right to left in Plate 2a. In $P_R(179)$, internal reflections occur down to about 2400 m, and there are reflections near the bed at depths between 2000 and 2300 m at SSE90. These layers correspond to the reflections that appear above the noise level near the bed in Plate 1(SSE90). We observed several examples of deep reflections near the subglacial peaks in the 1150-km long cross section, including this example. In $P_R(60)$, we can observe internal reflections down to about 2300 m. In a middle depth range (zone 1 in Plate 2a), the signal level tends to be weak, although in the same zone the signal level of $P_R(179)$ does not change. As a result, this zone appears on the ΔP_R image as a continuous zone of $\Delta P_R \simeq 10$ dB for more than 500-m of the thickness.

In Plate 2b, we can see changes in reflection amplitude above subglacial peaks and valleys in the vicinity of the dome summit. Around the dome, we cannot clearly identify the ice-flow direction. The ice thickness around the dome ranges between about 2300 and about 3300 m along several cross

sections across Dome Fuji. The Dome Fuji site is above a subglacial basin. Layers tend to be more nearly horizontal over the full 60 km width here compared with the other four sections of the ice sheet. However, we can observe that the irregular bed topography clearly extends toward shallower depths. The detection limit of $P_R(60)$ in the Z-scope display was about 1800 m, but for several hundred meters below this depth, there is a zone of $\Delta P_R \simeq 10$ dB (marked "zone 2" in Plate 2).

In Plate 2c, changes in reflection amplitude occur above a large subglacial peak. Ice flows from left to right in Plate 2c. The effect of the irregular and mountainous bed shape extends up to the surface through the layering. The level of the $P_R(60)$ signal does not change significantly between the upstream side (zone 3) and the downstream side (zone 4) of the subglacial peak, but the level of the $P_R(179)$ signal is stronger on the upstream side than on the downstream side. As a result, a zone of $\Delta P_R \simeq 10$ dB appears on the upstream side, and a zone of $\Delta P_R \simeq 0$ dB appears on the downstream side. We identified several more examples of this kind of contrast above the subglacial peaks in the inland area between SSE90 and MD364.

In Plate 2d, the $P_R(60)$ signal seems to disappear just below 1200 m, whereas the $P_R(179)$ signal is strong almost down to 1800-2000 m. As a result, a zone of $\Delta P_R \simeq 10$ dB appears in a depth range below about 1200 m (zone 5). Another interesting feature of $P_R(179)$ in this zone is that the signal level is stronger closer to the subglacial peaks (although it is not clear in Plate 2d). Below this zone, there is a basal echo-free zone as we saw in Plate 1 (MD298). Just as in Plate 2a, the $P_R(179)$ profile shows a few reflection layers near the bed at depths between 1500 and 2100 m. Another important feature of ΔP_R in this region is that there is no zone of $\Delta P_R \simeq 0$ dB on any downstream sides of the subglacial peaks, although the peaks of the bed distort the overlying layers just as in Plate 2c.

In Plate 2e, both $P_R(60)$ and $P_R(179)$ show detection limits at about 1500 m. The ΔP_R profile shows $\Delta P_R \simeq 10$ dB over all of the detected thickness. An interesting feature of the layers is that distinct layers are replaced by a 500-m-thick illuminated band in $P_R(179)$ (see zone 6).

3.3. Small-Scale Features

Another important feature that we observed is the pattern of successive reflecting layers. In all regions in the 1150-km-long cross section, layers at adjacent depths always appear nearly parallel, down to a scale as small as the pulse lengths of our measurement. On a large scale, however, we can find strains and folds in layers, as in the profiles in Plate 2. This small-scale feature characteristic is important in considering reflection mechanisms in the ice sheet. As for the continuity of the reflection layers, some are traceable over a distance longer than 100 km, and some are not. Whatever the continuity of the layers may be, adjacent ones are always subparallel, independent of depth ranges and regions in the ice sheet. There are no steps or jumps in layer separation, even at boundaries where ΔP_R changes between 0 dB and 10 dB. Only the intensity of each reflection layer changes along the traverse route.

4. Interpretation and Discussion

In this section, we will first discuss the existence and physical interpretation of the P_D, P_{COF}, C_A, and EF zones. From this, we interpret the structure of the ice sheet.

4.1. Physics of Four Zones and Their Boundaries

4.1.1. P_D, P_{COF}, or C_A zone?

Which of the three mechanisms, P_D, P_{COF}, or C_A dominates in the upper part of the ice sheet is determined by the relative strength of several factors. From the observations, we found that the upper 700-900 m of the ice sheet is dominated by $\Delta P_R \simeq 10$ dB without any exceptions. According to the basic principles that we developed, the primary cause of reflections in such a case is changes in permittivity, P_D. "P_D zone" simply means that P_D causes the strongest reflections, but this does not mean that the other mechanisms, C_A and P_{COF}, are completely absent. Indeed, the C_A mechanism surely must exist in the P_D zone, so long as isochrones are maintained. However, because of the dominance of the density fluctuations, the C_A mechanism is obscured.

Below the upper 700-900 m, some zones in the ice sheet are dominated by $\Delta P_R = 0$ dB and some are by $\Delta P_R = 10$ dB. Where $\Delta P_R = 0$ dB, the dominant reflection mechanism is changes in conductivity. We can therefore conclude that they are C_A zones.

Where $\Delta P_R = 10$, the dominant reflection mechanism is changes in permittivity. These are either P_{COF} or P_D zones. However, since they appear at a depth range around 2000 m in the vicinity of Dome Fuji (zone 2 in Plate 2) and extend to shallower depths (zones 1, 3, 5, and 6 in Plate 2), that cannot be explained by any density-related processes. They are far deeper than the deepest limit of the P_D mechanism (about 700-900 m). Therefore P_{COF} is the only possible mechanism. These considerations lead us to our interpretation of the dominant reflection mechanisms (Plate 1). Because the distribution of these zones and their boundaries are important indicators of the physical processes in the ice sheet, we next discuss the physical process which occurs in each case.

4.1.2. P_D/C_A boundary.

The boundary between these two zones is found at sites from SSE90 to MD364 at depths about 700-900 m. This boundary agrees well with the "zone of phase transition" (or transition zone), in which air bubbles change into clathrate hydrate crystals, as observed in several deep ice cores [e.g., Lipenkov, 1989; Shoji and Langway, 1982; Uchida et al., 1994]. In this zone, because hydrostatic pressure increases with depth, both the volume and the number of air bubbles decrease, and the number of clathrate hydrate crystals increases. In the case of the 2504-m Dome Fuji ice core, the transition zone was between about 500 m and 1000 m. Therefore we can interpret the P_D/C_A boundary as the approximate maximum depth for density fluctuation because of the existence of air bubbles causing dominant reflections. From a comparison with the ice core, it seems that the boundary exists roughly at the middle of the transition zone. In general, the depth range of the transition zone can vary from one region to another according to physical conditions like temperature, accumulation rate, and overburden pressure [e.g., Kameda et al., 1994; Shoji and Langway, 1982]. If this conclusion is correct, we should be able to investigate the variation of the transition-zone depth by detecting the P_D/C_A boundary at various sites.

4.1.3. P_{COF} zone.

Both the C_A and P_{COF} zones appear below the deepest limit of the P_D zone. What is the difference in physical processes between these two zones? The existence of the P_{COF} zone suggests that changes in crystal-orientation fabrics between adjacent layers exist in some limited depth ranges. In fact, discontinuous fluctuations of the crystal-orientation fabrics (of a vertical single-maximum pattern in

which the crystal axes (c axes) tend to be clustered around the vertical) were detected in the 2504-m ice core from Dome Fuji (N. Azuma, personal communication, 1998). Azuma carried out continuous measurement on several 1-m parts of the core with depth. He found that the cluster strength fluctuates dramatically even in a 1-m portion of the ice core. The single-maximum pattern can be developed by uniaxial compression and by shear strain [Azuma, 1994, 1995; Budd, 1972; Paterson, 1994; Russell-Head and Budd, 1979].

A question then arises as to what physical mechanism causes the changes in crystal-orientation fabrics between adjacent layers. The formation mechanism of the crystal-orientation fabrics has been discussed by many researchers and is attributed primarily to deformational history (recrystallization can also modify crystal-orientation fabrics) [see Paterson, 1994]. This implies that differences in deformational history must exist between adjacent layers. Since adjacent layers are under the same stress system, these differences in the deformational history could only come from differences in strain-rate in each layer. In addition, these adjacent layers are isochronous layers. For they can be traceable for a long distance, even though the reflection mechanism is different between depth ranges and between regions. Therefore we can infer that the reflections from the P_{COF} zone occur from the same series of layers as in the C_A zone. If the P_{COF} mechanism was not related to the isochronous structures, we should find some discontinuities between the parallelism of layers in the two zones. The nature of a single-maximum fabric pattern in the ice sheet supports this interpretation. Ice with a single-maximum fabric has anisotropic mechanical properties. The enhancement factor (the ratio of measured strain rate to that of isotropic ice at the same stress and temperature [Russell-Head and Budd, 1979]) can be up to 10 for simple shear and is less than 0.1 for the other stress configurations (e.g., uniaxial compression and pure shear) [e.g. Azuma, 1994, 1995]. The nature of the single-maximum pattern means that once it is developed, it enhances only additional properly oriented simple-shear strain and not any other strain component. In other words, once simple shear appears along horizontal planes (isochrones), the ice preserves that anisotropic structure during further deformation unless the stress system changes dramatically.

The next important question is, What mechanism primarily causes differences in strain rate between adjacent isochronous layers? The difference in the enhancement factor between ice-age ice and interglacial-age ice has been discussed by Paterson [1991]. This definition of the enhancement factor is slightly different from the original one by Russell-Head and Budd [1979]: it is the strain rate of ice-age ice relative to that of Holocene (interglacial age) ice under a particular shear stress and temperature. In his review, Paterson [1991] concluded that the initial ice viscosity, determined by chloride and possibly sulfate ions (components that tend to have higher concentration ice-age ice), can create initial differences in the enhancement factor and hence contrasts in the development of the single-maximum pattern between adjacent layers. The contrasts are developed further during additional deformation because the deformed ice is softer. Paterson also pointed out that this mechanism can explain the relatively small variations in the enhancement factor in the ice-age part of ice cores, such as those from Camp Century, Dye 3, and the Agassiz Ice Cap. Although there are still unknowns, there is

no direct evidence that can prove what impurities act and how they are present in the crystal-lattice, this kind of small-scale variation in the initial enhancement factor can amplify contrasts in the crystal-orientation fabrics. In order to clarify the initial mechanism, we need to investigate the correlation between crystal-orientation fabrics and chemical components from an ice core in the P_{COF} zone.

On the basis of the structure of the ice sheet we have discussed (stacking of isochronous layers that have different enhancement factors), we can propose a model for the ice sheet: (1) Strain occurs selectively because of the initial difference in enhancement factors; (2) deformed layers strain more readily because they are softer; (3) the dominant strain component is simple shear because of the anisotropic flow law of the single-maximum fabric; (4) isochronous surfaces are therefore preserved until the ice meets a stress component that can fold or mix it; and (5) we can observe the radar reflections due to changes in crystal-orientation fabrics from the ice where these conditions are satisfied. Finally, we can infer that the basic difference between the P_{COF} zone and the C_A zone to be whether or not the total strain is large enough to make contrasts in crystal-orientation fabrics. Therefore the P_{COF} zone is equivalent to the high-shear zone.

4.1.4. P_{COF}/C_A boundary above a subglacial peak.
The zone of $\Delta P_R \approx 10$ dB that appears upstream of the subglacial peaks (zone 3 in Plate 2) is a P_{COF} zone, whereas the zone of $\Delta P_R \approx 0$ dB downstream of the subglacial peaks (zone 4 in Plate 2) is a C_A zone. Although we cannot observe if there is diverging or converging flow around the peak from a Z-scope image alone, we found several examples of this P_{COF}/C_A boundary above a subglacial peak. This is an interesting feature that also suggests that the P_{COF} zone results from stress/strain configurations. The stress field around a bedrock peak has been analyzed by the two-dimensional model by Rowden-Rich and Wilson [1996]. They showed that stress concentration occurs in the ice mass as ice moves over the bedrock high and that stress relaxation occurs as the ice moves downward to a lee depression. Although the resolved stress system is too complex to describe here, these zones of stress localization and stress relaxation seem to agree with the P_{COF} zone and the C_A zone.

4.1.5. P_D/P_{COF} boundary.
ΔP_R is about 10 dB throughout the profile at sites between MD298 and H21 (Plate 1). Therefore it must be either a P_D zone or a P_{COF} zone. From the discussions above, the deepest limit of the P_D zone is somewhere in the transition zone, about 700-900 m (indicated as "P_D limit" in Plate 1 in sections MD364 and MD298). The present measurements cannot in principle show a clear boundary between the P_D and P_{COF} zones.

4.1.6. Basal Echo-free zone and its boundary with P_{COF}.
The basal echo-free (EF) zone, several hundred meters thick, appears always below a P_{COF} zone, clearly seen as "EFZ" in Plate 1 (MD364 and Mizuho). At the sudden drops (SD) of P_R the gradient (dP_R/dz) is about 10 times larger than the gradient at depths above the SD. This sudden drop can be explained only by sudden changes in power reflection coefficients and not sudden changes in the loss factor L in (2). If it were due to changes in L, it could be explained only by a sudden change in ice temperature of about 20° at the boundary, considering the temperature dependence of dielectric loss in ice [T. Matsuoka et al., 1996], which is not realistic. The EF zone was first discovered by Robin et al. [1977], and it was discussed by Robin and Millar [1982]. They found that the

thickness of the EF zone tends to increase away from the crest of Dome B in East Antarctica and suggested that the transition between shear controlled by bedrock surfaces and shear controlled internally due to the mean surface slope takes place at a relatively sharp boundary around the upper limit of the EF zone. The observation in this study tends to support this idea.

An "echo-free" scenario is as follows. In the EF zone, ice cannot release stresses by slip deformations along isochrones because the shear is controlled by the irregular surface of the bedrock. These shear-strain components instead cause folding, mixing, and faulting of layers. As a result, no coherent radar return appears. Furthermore, under these conditions, shear-strain components do not agree with the "easy glide planes" of the ice sheet, that is, isochrones, so the enhancement factor should be very small. Considering the fact that the anisotropic flow law proposed by Azuma [1994, 1995] predicts that the enhancement factor is different by more than an order of magnitude between simple shear and other stress/strain systems, the EF zone seems to be composed of stagnant ice. From our experiment, we cannot finally determine whether the EF zone is stagnant because of the lack of velocity data along our traverse line.

However, field measurements in some other regions in Antarctica suggest that there is stagnant ice near the bed. Russell-Head and Budd [1979] presented field evidence of basal stagnant ice accompanied by a high-shear zone above it. They examined field evidence of the velocity profile, crystal-orientation fabrics profile, and/or an ultrasonic velocity profile at Law Dome [Russell-Head and Budd, 1979] and at Byrd station [Bentley, 1972; Garfield and Ueda, 1976; Gow and Williamson 1976]. Russell-Head and Budd [1979] concluded that (1) there may be a widespread, rather immobile (or stagnant) layer as the base of the ice sheet, (2) the shear stress decreases toward the bed after reaching a maximum in the layer of the high-shear layer located at the depth of about two thirds of the ice thickness, and (3) the high concentration of vertical single-maximum c axis is a result of the high horizontal shear stress, while the large-crystal ice results from a type of annealing process associated with the lower shear stress and higher temperature toward the base. It appears that their observations and interpretations explain the contrast between the EF zone and the P_{COF} zone above it. In particular, an annealing process can completely mute the changes in crystal-orientation fabrics. If this process occurs, reflections do not occur from within the ice. It therefore appears that in the EF zone the cause of reflection does not exist and that, even if the cause can still exist at some parts, coherent waves cannot appear from there.

The sharp boundary between the P_{COF} zone and the EF zone means that there is a critical physical condition that separates the ice into these two zones. It could be a function of several factors: the ratio between horizontal and vertical shear stress components, relatively higher temperatures near the bed, and the age of the ice, because all of these influence the flow regime, the flow law, and the process of crystalline fabric formation. Finding a clear description of this critical condition is an important task for realistic ice sheet modeling.

4.2. Distribution of the Zones and Its Implications for Ice Sheet Dynamics

Following the discussion of each zone, we discuss in this section the distribution of the zones in the ice sheet and its relation to ice sheet dynamics.
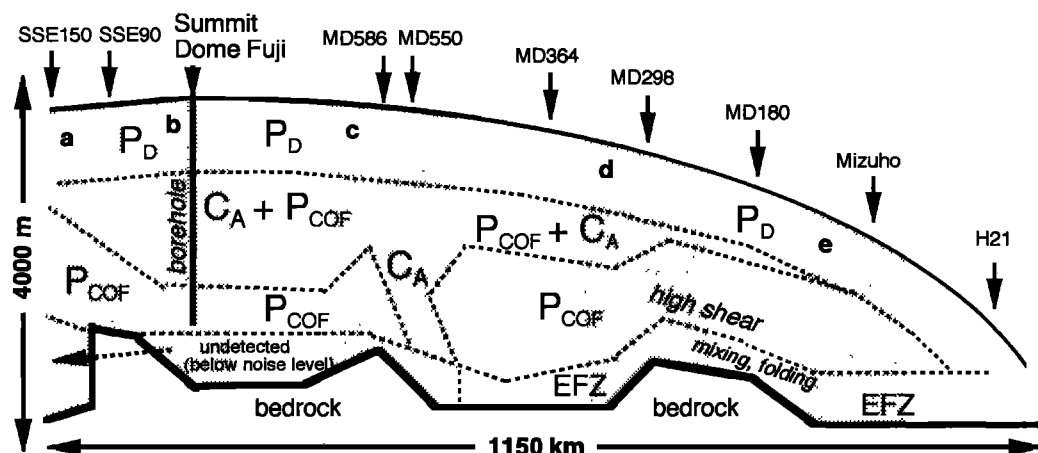
Figure 3. Schematic map interpretation of the dominant radio echo reflection mechanisms from the dome summit area to the coast. Sections a-e of Figures 1 and 2, and Plate 2 are shaded.

4.2.1 General features of the ice sheet. From the results (Plate 1 and 2) and the interpretation of the radar profiles, we tentatively propose an internal structure map of the ice sheet (Figure 3) which schematically depicts the dominant reflection mechanisms in each region and the depth ranges.

In agreement with previous studies, the P_D zone covers the upper several hundred meters of the entire ice sheet, approximately down to 700-900 m. Below it, there is a depth range in which either the C_A mechanism or the P_{COF} mechanism dominates. The depth range of a few to several hundred meters above the bed corresponds to the EF zone or a zone where we simply could not detect the significant signal level to determine reflection mechanisms (BDL). Above the EF zone, there is a P_{COF} zone. Between this deepest P_{COF} zone and the P_D zone, both C_A zones and P_{COF} zones appear (see sites from SSE150 to MD586 in Plate 1, for example). The C_A zones are thicker around the Dome Fuji area and at several sites downstream of the subglacial peaks (see MD550, for example). This kind of thick C_A zone appears only in areas between SSE90 and MD364. However, as we go closer to the coast, P_{COF} zones tend to dominate at sites downstream of subglacial peaks. At Dome Fuji, the P_{COF} zone appears over a depth range of around 2000 m and extends to lesser depths away from the dome, as in zones 1, 5, and 6 in Plate 2.

4.2.2. Stress/strain system at Dome Fuji. At Dome Fuji, in the depth range between 700 and 1700 m, the C_A zone dominates. This observation can be related to a stress/strain regime around the dome summit. The deformation in ice in the vicinity of ice divides has been analyzed by several researchers [e.g., Hvidberg, 1996; Raymond, 1983]. Their model-based analyses showed consistent results as follows. The ice-divide zone is a narrow region, only several ice thicknesses wide, where the surface slope drops to zero and the flow solution changes. The longitudinal strain rate is high, especially in the upper layers, and the vertical velocity is smaller than away from the divide. Horizontal shear strain increases gradually down to the bed. It is less concentrated at the center of the ice divide than in the flanks. An important difference between the assumptions of these model-based analyses and the actual condition of Dome Fuji is that the it has irregularities in the bed of more than 500 m (one sixth of

the ice thickness), whereas the models commonly assume a flat bed.

We interpret the C_A zone and the P_{COF} zone below about 1700 m (zone 2 in Plate 2) as follows. Because of the less concentrated horizontal shear strain at the dome, the differential movement of the selective layers, which causes the contrast of crystal-orientation fabrics between adjacent layers, is less active. However, this contrast increases with depth because of the increase of the simple-shear strain component down to the bed. Since we observed several peaks and troughs in the same depth range along several other cross sections across Dome Fuji, we conclude that the ice below about 2500 m is stagnant. Thus we can consider that the depth range around 2500 m is effectively the bed of the mobile part of the ice. Ice just above 2500 m should have the highest shear strain rate. On the other hand, according to electrical conductivity measurements along the Dome Fuji ice core, prominent conductivity peaks do not appear below about 2000 m, probably owing to diffusion of impurity ions, thinning of each annual layer, and/or a muting effect due to cations [Taylor et al., 1993]. Therefore we interpret the appearance of the P_{COF} zone below about 1700 m basically as a result of both the increase of the shear strain component with depth and the absence of the C_A mechanism. Possible migration of the dome position should be examined in further analysis.

4.2.3. Growth of high-shear zones. The distribution of the P_{COF} zone reveals some interesting dynamical features in the ice sheet. Southward from Dome Fuji, the P_{COF} zone extends gradually to higher levels (see zone 1 in Plate 2a). This means that an active shear zone, which appears first above a bedrock rise, also extends far above the bed in this region because of the continuous ice flow from upstream. Appearance of the reflections near the bed (see SSE90 in Plate 1 and 2a) also suggests that a high-shear zone exists there. In addition, appearance of the reflection means that isochronous surfaces still exist there and that they slip to release internal stresses. If an isochronous structure did not exist, as in the EF zone, this deep reflector would never appear.

The shear zone (zone 1 in Plate 2a) ranges over ages of ice between about 50,000 and 350,000 years old, estimated from the timescale for the Dome Fuji core and several traceable layers between Dome Fuji and zone 1. This suggests that the

distribution of glacial and interglacial ice (for example, the Eemian (last interglacial age ice) is around 1600-1700 m in this region) is not of primary importance to the distribution of the high-shear zone. Both ice-age ice and interglacial-age ice can be either a C_A zone or a P_{COF} zone.

Farther downstream, the data show high-shear zones in the middle depth range (see zones 5 and 6 in Plate 2). The Z-scope data show that the reflection is stronger upstream of the bedrock rises (zone 5). The strong upward inclination of the reflection layers suggests that the shear strain has an upward component. The upward stress component can appear because of the occurrence of a compressive longitudinal stress due to the bedrock rise. This interpretation is consistent with the observational fact that the ice sheet surface at MD298 is an ablation zone (surface mass balance is negative), which means that there is an upward flow component. Near Mizuho station, the high-shear zone appears as a wide band at depths between 1000 m and 1500 m (zone 6 in Plate 2). By correlating the age of the ice column between the Dome Fuji ice and Mizuho Station using several traceable reflection layers, we tentatively concluded that the age of the ice ranges between about 20,000 and 70,000 years. This estimate of the age is consistent with the age of the 700-m Mizuho station core covering about 9400 years [*Nakawo et al.*, 1989]. It means that zone 6 corresponds to the Wisconsin-age ice. A simple interpretation of this fact is that ice-age ice may constitute the zones of actual shear displacement around Mizuho station, where thinning of the ice sheet has been observed in the vicinity [*Mae and Naruse*, 1978].

5. Conclusions

Through the two-frequency radar experiments, three reflection mechanisms, P_D, P_{COF}, and C_A, were identified in the ice sheet in different regions and depth ranges. Additionally, a basal echo-free zone was found generally below a P_{COF} zone. These four zones and their distribution suggest variations of the physical conditions in the ice sheet. In particular, the P_{COF} zone is an indicator of simple-shear strain parallel to the isochrones. Distribution of the P_{COF} and the EF zone suggested to us variations of the flow regimes in the ice sheet. Whatever the reflection mechanism, the reflections still all reveal isochrones.

We have demonstrated that multifrequency radar sounding is a useful method for clarifying the internal nature of the ice sheets. We believe that other frequencies besides our two (60 and 179 MHz) can provide considerable information on the extent of conductivity- and permittivity-based reflections. Ice radar is not only a tool to detect boundary conditions of ice sheets (surface, bed, and isochrones) but is also a tool which reveals internal physical processes.

References

Ackley, S. F., and T. E. Keliher, Ice sheet internal radio-echo reflections and associated physical property changes with depth, *J. Geophys. Res.*, *84*(B10), 5675-5680, 1979.

Azuma, N., A flow law for anisotropic ice and its application to ice sheets, *Earth Planet. Sci. Lett.*, *128*, 601-614, 1994.

Azuma, N., A flow law for anisotropic polycrystalline ice under uniaxial compressive deformation, *Cold Reg. Sci. and Technol.*, *23*, 137-147, 1995.

Bailey, J. T., S. Evans, and G. de Q. Robin, Radio echo sounding of polar ice sheets, *Nature*, *204*, 420-421, 1964.

Bentley, C. R., Seismic-wave velocities in anisotropic ice: A comparison of measured and calculated values in and around the deep drill hole at Byrd Station, Antarctica, *J. Geophys. Res.*, *77*(23), 4406-4420, 1972.

Bogorodskiy, V. V., C. R. Bentley, and P. E. Gudmandsen, *Radioglaciology*, D. Reidel, Norwell, Mass., 1985.

Budd, W. F., The development of crystal orientation fabrics in moving ice, *Z.Gletscherk. Glazialgeol. 8*, 65-105, 1972.

Clough, J. W., Radio-echo sounding: Reflection from internal layers in ice sheets, *J. Glaciol. 18*(78), 3-14, 1977.

Evans, S., Dielectric properties of ice and snow-A review, *J. Glaciol.*, *5*(42), 773-792, 1965.

Fujita, S., and S. Mae, Causes and nature of ice sheet radio-echo internal reflections estimated from the dielectric properties of ice, *Ann. Glaciol.*, *20*, 80-86, 1994.

Fujita, S., M. Shiraishi, and S. Mae, Measurement on the dielectric properties of acid-doped ice at 9.7 GHz, *IEEE Trans. Geosci. Remote Sens.*, *30*(4), 799-803, 1992a.

Fujita, S., M. Shiraishi, and S. Mae, Measurement on the microwave dielectric constant of ice by the standing wave method, *The Proceedings of the International Symposium on the Physics and Chemistry of Ice, (Edited by N. Maeno, and T. Hondoh,)*, Hokkaido University Press, Sapporo, 415-421, 1992b.

Fujita, S., S. Mae, and T. Matsuoka, Dielectric anisotropy in ice Ih at 9.7 GHz., *Ann. Glaciol.*, *17*, 276-280, 1993.

Garfield, D. E., and H. T. Ueda, Resurvey of the "Byrd" Station, Antarctica, drill hole, *J. Glaciol.*, *17*(75), 29-34, 1976.

Gow, A. J., and T. Williamson, Rheological implications of the structure and crystal fabrics of the West Antarctic Ice Sheet as revealed by deep core drilling at Byrd Station, *Geol. Soc. Am. Bull. 87*(12), 1665-1677, 1976.

Gudmandsen P., Layer echoes in polar ice sheets, *J. Glaciol.*, *15*(73), 95-101 1975.

Hammer, C. U., Acidity of polar ice cores in relation to absolute dating, past volcanism, and radio echoes, *J. Glaciol.*, *25*(93), 359-372, 1980.

Harrison, C. H., Radio echo sounding of horizontal layers in ice, *J. Glaciol.*, *12*(66), 383-397, 1973.

Hvidberg, C. S., Steady-state thermomechanical modelling of ice flow near the centre of large ice sheets with the finite element technique, *Ann. Glaciol.*, *23*, 116-123, 1996.

Jacobel, R. W., and S. M. Hodge, Radar internal layers from the Greenland summit, *Geophys. Res. Lett.*, *22*(5), 587-590, 1995.

Kameda, T., H. Shoji, K. Kawada, O. Watanabe, and H. B. Clausen, An empirical relation between overburden pressure and firn density, *Ann. Glaciol.*, *20*, 87-94, 1994.

Lipenkov, V. Y., Formation and decomposition of air hydrates in glacier ice (in Russian), *Mater. Glyatsiol. Issled.*, *65*, 58-64, 1989.

Mae, S., and R. Naruse, Possible causes of ice sheet thinning in the Mizuho Plateau, *Nature*, *273*, 291-292, 1978.

Maeno, H., K Kamiyama, T. Furukawa, O. Watanabe, R. Naruse, K. Okamoto, T. Suitz, and S. Uratsuka, Using a mobile radio echo sounder to measure bedrock topography in East Queen Maud Land, Antarctica, *Proc. NIPR Symp. Polar Meteorol. Glaciol.*, *8*, 149-160, 1994.

Maeno, H., S. Uratsuka, K. Okamoto, and O. Watanabe, Subsurface survey of the Antarctic ice sheet using a mobile radio-echo sounder, *J. Communi. Res. Lab.*, *43*(2), 139-149, 1996.

Matsuoka, K., S. Fujita, T. Matsuoka, T. Ishida, T. Hondoh, and S. Mae, Measurement of the complex permittivity of acid-doped ice from 1 kHz to 30 MHz - New data set for developing ice radar and dielectric analysis of ice cores -, *Proc. NIPR Symp. Polar Meteorol. Glaciol.*, *10*, 25-35, 1996.

Matsuoka, T., S. Fujita, and S. Mae, Effect of temperature on dielectric

properties of ice in the range 5-39 GHz, *J. Applied Phys.*, *80*(10), 5884-5890, 1996.

Matsuoka, T., S. Fujita, and S. Mae, Dielectric properties of ice containing ionic impurities at microwave frequencies, *J. Phys. Chemi. B*, *101*(32), 6219-6222, 1997a.

Matsuoka, T., S. Fujita, S. Morishima, and S. Mae, Precise measurement of dielectric anisotropy in ice Ih at 39 GHz, *J. Applied Phys.*, *81*(5), 2344-2348, 1997b.

Millar, D. H. M., Radio-echo layering in polar ice sheets and past volcanic activity, *Nature*, *292*, 441-443, 1981.

Miners, W. D., A. Hildebrand, S. Gerland, N. Blindow, D. Steinhage, and E. W. Wolff, Forward modeling of the internal layers in radio echo sounding using electrical and density measurements from ice cores, *J. Phys. Chem. B*, *101(32)*, 6201-6204, 1997.

Moore, J. C., Dielectric variability of a 130 m Antarctic ice core: Implications for radar sounding, *Ann. Glaciol.*, *11*, 95-99, 1988.

Moore, J. C., and S. Fujita, Dielectric properties of ice containing acid and salt impurity at microwave and low frequencies, *J. Geophys. Res.*, *98*(B6), 9769-9780, 1993.

Nakawo, M., H. Ohmae, F. Nishio, and T. Kameda, Dating the Mizuho 700-m core from core ice fabric data, *Proc. NIPR Symp. Polar Meteorol. Glaciol.*, *2*, 105-110, 1989.

Paren, J. G., Reflection coefficient at a dielectric interface, *J. Glaciol.*, *27*(95), 203-204, 1981.

Paren, J. G., and G. de Q. Robin, Internal reflections in polar ice sheets, *J. Glaciol.*, *14*(71), 251-259, 1975.

Paterson, W. S. B., Why ice-age ice is sometimes "soft", *Cold Reg. Sci. Technol.*, *20*, 75-98, 1991.

Paterson, W. S. B., *The Physics of Glaciers*, Pergamon, Tarry town, N. Y.,1994.

Raymond, C. F., Deformation in the vicinity of ice divide, *J. Glaciol.*, *29*(103), 357-373, 1983.

Robin, G. de Q., Radio-echo sounding: Glaciological interpretations and applications, *J. Glaciol.*, *15*(73), 49-64, 1975.

Robin, G. de Q., and D. H. M. Millar, Flow of ice sheets in the vicinity of subglacial peaks, *Ann. Glaciol.*, *3*, 290-294, 1982.

Robin, G. de Q., S. Evans, and J. T. Bailey, Interpretation of radio echo sounding in polar ice sheets, *Philos. Trans. R. Soc. London, Ser. A*, *265*(166), 437-505, 1969.

Robin, G. de Q., D. J. Drewry, and D. T. Meldrum, International studies of ice sheet and bedrock, *Philos. Trans. R. Soc. London, Ser. B*, *279*(963), 185-196, 1977.

Rowden-Rich, R. J. M., and C. J. L. Wilson, Models for strain localization in Law Dome, Antarctica, *Ann. Glaciol.*, *23*, 396-401, 1996.

Russell-Head, D. S., and W.F. Budd, Ice-sheet flow properties derived from bore-hole shear measurements combined with ice-core studies, *J. Glaciol.*, *24*(90), 117-130, 1979.

Shoji, H., and C. C. Langway Jr., Air hydrate inclusions in fresh ice core, *Nature*, *298*, 548-550, 1982.

Taylor, K. C., C. U. Hammer, R. B. Alley, H. B. Clausen, D. Dahl-Jensen, A. J. Gow, N. S. Gundestrup, J. Kipfstuhl, J. C. Moore, and E. D. Waddington, Electrical conductivity measurements from the GISP2 and GRIP Greenland ice cores, *Nature*, *366*, 549-552, 1993.

Uchida, T., P. Duval, V. Y. Lipenkov, T. Hondoh, and S. Mae, Brittle zone and air-hydrate formation in polar ice sheets, *Mem. Natl. Inst. Polar Res., Speci. Issue Jpn.*, *49*, 298-305, 1994.

Ulaby, F. T., R. K. Moore, and A. K. Fung, *Microwave Remote Sensing: Active and Passive*, pp. 925-966, Addison-Wesley, Reading, Massachusetts, 1982.

Warren, S. G., Optical constants of ice from the ultraviolet to the microwave, *Appl. Opt.*, *23*, 1206-1225, 1984.

Y. Fujii, T. Furukawa, and O. Watanebe, National Institute of Polar Research , 1-9-10, Kaga, Itabashi-ku, Tokyo, 173-8515, Japan. (e-mail: fujii@pmg.nipr.ac.jp, furukawa@nipr.ac.jp, watanabe@nipr.ac.jp)

S. Fujita and S. Mae, Department of Applied Physics, Faculty of Engineering, Hokkaido University, Sapporo, 060-8628, Japan. (e-mail: sfujita@nd-ap.eng.hokudai.ac.jp, mae@nd-ap.eng.hokudai.ac.jp)

H. Maeno and S. Uratsuka, Communications Research Laboratory, Ministry of Post, Nukui-Kita-machi, Koganei, Tokyo, 184-0015, Japan. (e-mail: maeno@crl.go.jp, pata@crl.go.jp)